On the Role of Deformation and Cracking in the Cold Spray Processing of Refractory Ta Powders Onto Ta or 4340 Steel Substrates: Effects of Topical Oxide Layers and Spray Velocity

R.A. AHMED, V. RAHNESHIN, T. BOND, M. VANDADI, J.E. OGHENEVWETA, A. NAVABI, O.K. OYEWOLE, J.D. OBAYEMI, N. RAHBAR, and W.O. SOBOYEJO

This paper presents the results of a combined experimental and computational study of the role of deformation and cracking phenomena on the cold spray processing of refractory Ta powders with topical nanoscale oxide layers. The structure of the Ta powders and the topical nanoscale oxide films are elucidated using a combination of Scanning Electron Microscopy (SEM), Focused Ion Beam (FIB) and Transmission Electron Microscopy (TEM). The mechanical properties of the topical oxides are also obtained from *ab-initio* density functional theory (DFT) calculations. The results obtained from DFT and SEM/TEM measurements of film dimensions are then incorporated into the finite element (FE) models of deformation, heating, and cracking phenomena. The induced temperatures and stresses associated with the cold spray impact of Ta particles with Ta or 4340 steel substrates are then discussed along with their implications for the development of splat microstructures, cracking, and the design of cold spray conditions for the fabrication and repair of robust Ta and 4340 steel structures.

I. INTRODUCTION

COLD spray (CS) technology is a rapidly emerging processing technique which shares some similarities with the conventional thermal spray technique.[1] This technique involves the deposition of powder particles or suspension at sub or supersonic velocity (300 to 1200 ms^{-1}) on a substrate near ambient temperature.[2–4] In contrast to the traditional thermal spray technique, deposits or coatings are realized without melting the materials involved in the cold spray process.[2,5]

Cold spray is cost effective and suitable for large scale fabrication and repair.[4] This technique has been adopted for the repair of corroded and damaged metal parts.[6,7] It has also been demonstrated as a viable method for the processing of polymer coatings[8,9] as well as electrode materials for energy applications.[10–15]

Adhesion occurs during CS when the kinetic energy of the particle is dissipated upon impact at the substrate. Some authors have attributed the bonding in CS to 'adiabatic shear instability'.[16,17] This is a phenomenon in which the heat generated by high impact during cold spray causes a reduction in the flow stress, which results in a localized deformation of the powder into a splat and jetting. Others have claimed that adiabatic shear instability is not necessary for bonding and have attributed the bonding to hydrodynamic plasticity process.[18,19] According to this hypothesis, the critical velocity is strongly related to the bulk speed of sound in the material. Jetting is also believed to remove oxides and surface asperities to allow for metallic bonding.[18,19]

Prior studies have suggested that nanoscale oxide and hydroxide layers are formed on powder and substrate surfaces during storage or exposure to ambient atmospheres. These may influence the cold spray behavior of metallic particles[20–25] during cold spray processing and repair. Furthermore, in recent times, there has been increasing interest in the cold spray of refractory metal powders, such as Ta.[26–28] This is because Ta exhibits an exceptional combination of mechanical properties and corrosion resistance at ambient and high temperatures.

R.A. AHMED, T. BOND, J.E. OGHENEVWETA, O.K. OYEWOLE, J.D. OBAYEMI, and W.O. SOBOYEJO are with the Materials Science and Engineering Program, Department of Mechanical Engineering, Worcester Polytechnic Institute, Worcester, MA 01609. Contact e-mail: wsoboyejo@wpi.edu V. RAHNESHIN is with the Materials Science and Engineering Program, Department of Mechanical Engineering, Worcester Polytechnic Institute and also with the Department of Civil and Environmental Engineering, Worcester Polytechnic Institute, Worcester, MA 01609. M. VANDADI, A. NAVABI, and N. RAHBAR is with the Department of Civil and Environmental Engineering, Worcester Polytechnic Institute.
Manuscript submitted March 9, 2022; accepted June 17, 2022.
Article published online July 1, 2022

Hence, Ta has been recognized by the aerospace, defense, and energy industries as an important material for applications that require a balance of long-term mechanical integrity and chemical stability.[29]

However, the roles of topical surface oxide layers (formed on the surface of Ta metal) and topical oxides on possible Ta and steel substrates have not been studied in detail under cold spray conditions. Furthermore, the possible effects of cold spray velocity are yet to be fully explored for the cold spray of Ta powders onto similar or dissimilar substrates.

In this work, we present the results of a combined experimental and theoretical/computational study of the deformation and cracking phenomena associated with the cold spray of Ta powders with nanoscale topical oxide layers. A combination of density functional theory (DFT) and finite element modeling is used to study the deformation and cracking. Mechanical properties obtained from DFT calculations are used in finite element simulations that are used to study the induced stresses that are associated with the cold spray of Ta onto Ta or 4340 steel substrates. The effects of topical oxide layers are also examined before discussing the implications of the results for the design and repair of refractory Ta and 4340 steel structures.

II. MATERIALS AND METHODS

A. *Materials Characterization*

The tantalum powders that were used in this study were obtained from VRC Inc. Webster, MA. The microstructure of the powder particles and the structure of the top surface oxide were characterized using a scanning electron microscope (SEM) (JEOL, JSM-700F Field Emission Scanning Electron Microscope, Tokyo, Japan), focused ion beam (FIB) and transmission electron microscope (TEM). The size distribution of the Ta powder particles was obtained using ImageJ software package (Image J, NIH, Bethesda, MD).

Figures 1(a) and (b) present the SEM images of the powder particles, while a histogram of the size distribution of the Ta powder particles is plotted and presented in Figure 1(c). The particle size is in the range between 2 and 20 μm, with a mean particle size of 10.9 μm.

Bright-field transmission electron microscopy (BF-TEM) and Bright-field scanning transmission electron microscopy (BF-STEM) images of the deposited C/Pt layer (~ 250 nm thick) and the Ta particulate powder substrate are presented in Figures 2(a) and (b), respectively. High-angle annular dark-field (HAADF) microstructures obtained from a FIB-cut cross section through the surface of Ta powder are also presented in Figures 2(c) and (d). These show regions of deposition layers, while the Ta powder substrate particle and the outer oxide layer clearly reveal the presence of an amorphous oxide layer on the Ta particle with a thickness of 2.8 $\pm$ 0.01 nm. A d-spacing of ~ 0.234 nm between the (110) crystallographic planes of Ta substrate is revealed by the HAADF microstructure shown in Figure 2(d).

The scanning transmission electron microscopy-energy dispersive X-ray analysis (STEM-EDAX) results obtained from a FIB-cut cross section through the surface of Ta powder particle are also presented in Figures 3(a) and (b), while the X-ray maps showing the elemental compositions that are extracted from Figures 3(a) and (b) are shown in Figures (i through vi).

B. *Computational Modeling*

1. *Density functional theory calculations*

The mechanical properties of the top surface oxides on the 4340 steel substrate were obtained from first-principles calculations. This method has been successfully used to calculate the mechanical properties of oxides by previous authors.[30–32] The calculations were carried out using density functional theory (DFT) as implemented in Quantum ESPRESSO.[33] The exchange-correlation potential was treated in the generalized gradient approximation (GGA) of Perdew–Burke–Ernzerhof (PBE).

DFT + U was employed, where the PBE exchange-correlation functional was combined with a Hubbard U (U_{eff} = 4.3 eV) to treat the strongly correlated Fe 3d electrons.[34] This functional was chosen because it has been shown to produce bulk lattice constants that are in good agreement with experiments.[35] Also, all calculations were spin polarized because of the antiferromagnetic nature of Fe_2O_3. For simplicity and to avoid convergence problem, the primitive cell of Fe_2O_3 was used for the DFT calculations. The structures of the oxides considered in the DFT calculations are shown in Figures 4(a) and (b).

Test calculations show convergence of the numerical results at 750 eV (Fe_2O_3) plane wave cut-off energy combined with 5 $\times$ 5 $\times$ 5 (Fe_2O_3) $\vec{k}$-meshes. A 10^{-7} eV total energy convergence criterion and a 0.001 eV/Å force convergence criterion were used for the structure relaxations. The mechanical properties of the oxides were computed using Thermo_pw*. This computes the

*Thermo_pw is a set of FORTRAN drivers of the Quantum ESPRESSO routines that help to speed up the most common tasks. The mechanical properties reported in this paper were calculated with the scf_elastic_constant and mur_lc_elastic_constant options. See https://dalcorso.github.io/thermo_pw/.

nonzero stress tensor components for a set of strains and derives the elastic constants from the numerical first derivative of the stress with respect to strain. The code then computes and output a few auxiliary numbers using the elastic constants tensor: the bulk modulus, the poly-crystalline averages of the Young's modulus, the shear modulus, and the Poisson's ratio.

2. *Finite element models*

The cold spray behavior of Ta particle deposited on a Ta substrate, and on a 4340 steel substrate was described by a finite element model of a single particle impact that includes the topical oxides on both the particle and the substrate. All simulations were carried out in
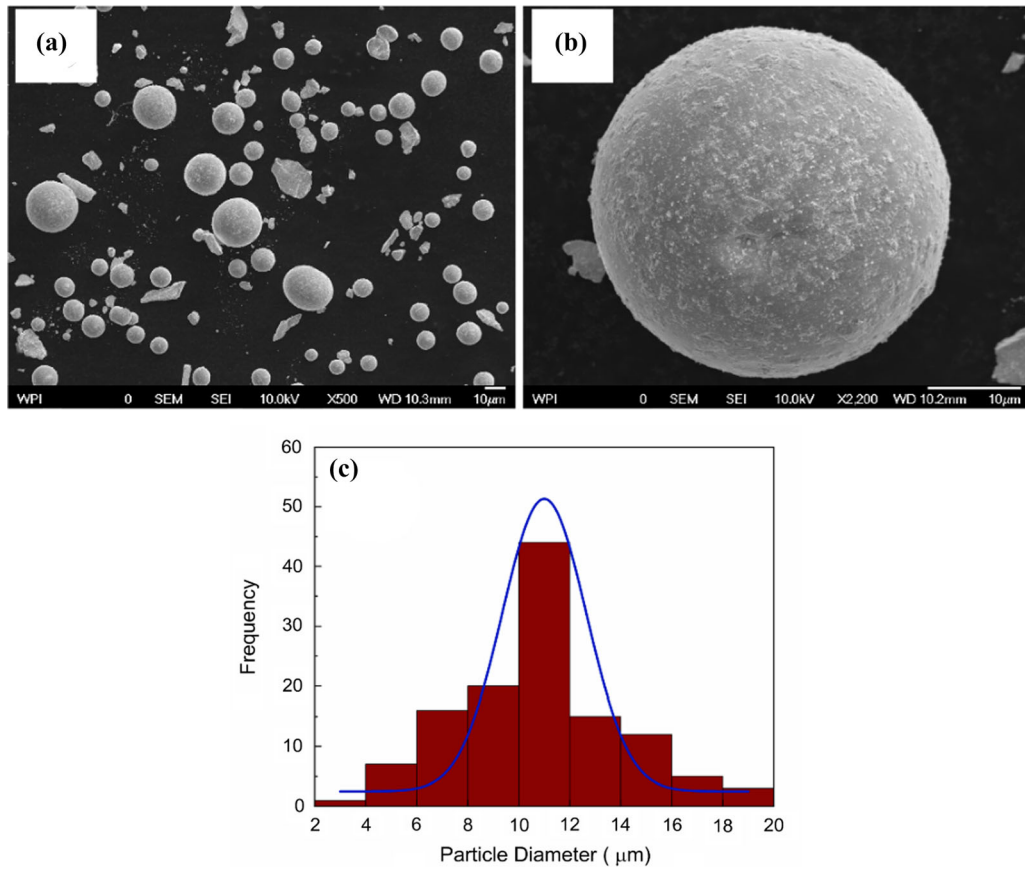
Fig. 1—(*a, b*) SEM images of the Ta powder particles (*c*) particle size distribution of Tantalum powder.

ABAQUS-Explicit where a hard contact was assumed between the layers while the topical oxides were modeled as shells tied to the particle (Ta) or the substrate (Ta, 4340 steel).

An axisymmetric geometry of a perfectly spherical Ta particle on a cylindrical shaped substrate with flat surface was assumed. Hexagonal and tetragonal elements were used for the substrate and particle meshes, respectively, with the element size equal to $\frac{1}{30}d_p$, where d_p is the diameter of the particle chosen to be 10 μm, in accordance with the result obtained in Figure 1. Shell elements with seed size equal to $\frac{1}{50}d_p$ were used for the oxide layer.

The substrate lateral sides were subjected to a symmetry boundary condition, and the substrate bottom was constrained against all degrees of freedom. The particle and substrate initial temperature were set to 298 K at the start. The starting particle velocity was set at 680 ms^{-1}, a value estimated from the simple formula of critical velocity (Eq. [1]) proposed in Reference 36. This is consistent with the result presented in Reference 37 in which critical velocity for Ta with a diameter of 25 μm was estimated to be 500 ms^{-1}. Since the critical velocity increases with decrease in particle size,[37,38] a value of 680 ms^{-1} estimated for 10 μm Ta particle is reasonable for Ta powders with an average diameter of about 10 μm.

$$v_{cr} = 667 - 14\rho + 0.08T_m + 0.1\sigma_u - 0.4T_i, \qquad [1]$$

where ρ is the density (gcm^{-3}), T_m is the melting temperature in °C, σ_u is the ultimate strength in MPa, and T_i is the initial temperature of the particle in °C.

3. *Deformation model*

The conventional Johnson-Cook (JC) plasticity model has been shown to underestimate the flow stress for high strain rates.[39,40] Thus, to accurately capture the flow stress in the ultra-high strain rate regime in cold spray impact, a modified model which gives a better estimate of the flow stress is necessary. In this work, a custom Bilinear Johnson–Cook (BJC) plasticity model was developed using VUMAT (a user subroutine to develop material behavior in ABAQUS)[41] to achieve a better approximation of the strain rate sensitivity in the constitutive model for the higher strain rate domain.

In BJC model, an additional strain rate constitutive term (C_2) is added to the linear JC and prior research has demonstrated that experimental data on flow stress may be adequately represented by the inclusion of this C_2 term.[42] The Bilinear Johnson-Cook (BJC) equation is presented in Eqs. [2] and [3].

$$\sigma = (A + B\varepsilon^n)\left[1 + C ln\left(1 + \frac{\dot{\varepsilon}}{\dot{\varepsilon}_0}\right)\right]\left[1 - \left(\frac{T - T_r}{T_m - T_r}\right)^m\right] \qquad [2]$$
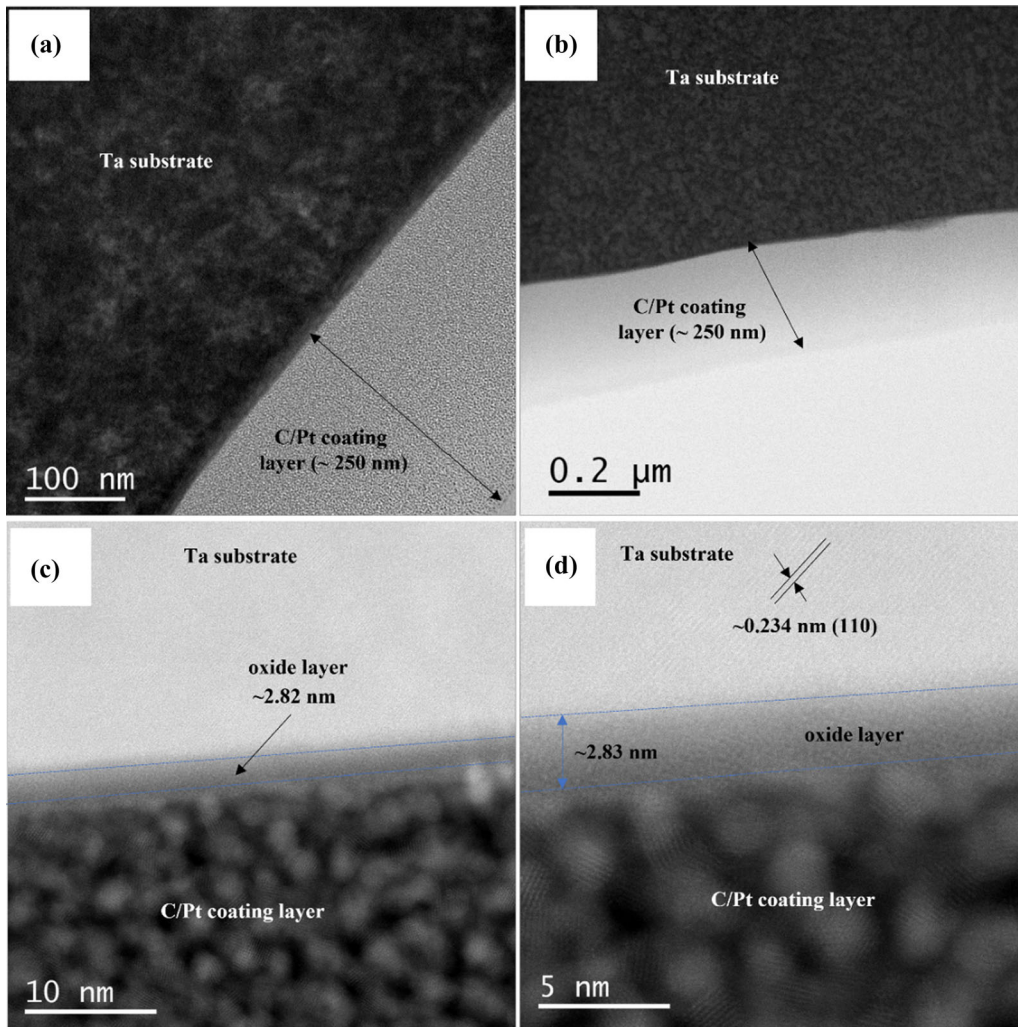
Fig. 2—(a) BF-TEM image showing regions of deposition C/Pt layer (~ 250 nm thick) and the Ta powder substrate particle, and (b) BF-STEM image showing corresponding low magnification of the deposition layer and the Ta powder substrate particle. HAADF microstructures obtained from a FIB-cut cross section through the surface of Ta powder particle showing (c) low magnification revealing regions of deposition layers and the Ta powder substrate particle, and the outer oxide layer, (d) Higher magnification of image revealing the distinct outer oxide layer thickness (~ 2.83 nm thick).

$$C = \left\{ \begin{array}{ll} C_1 & \dot{\varepsilon}_p < \dot{\varepsilon}_c \\ C_2 & \dot{\varepsilon}_p \geq \dot{\varepsilon}_c \end{array} \right\}, \qquad [3]$$

where $A, B, n, C,$ and m are materials constants, the values of which are presented in Table I. Also, T is temperature of material, T_r is reference temperature, T_m is melting temperature, ε is strain, $\dot{\varepsilon}$ is strain rate and $\dot{\varepsilon}_0$ is reference strain rate.

The dynamic failure used in the model is presented in Eqs. [4] and [5]

$$\omega = \sum \left(\frac{\Delta \bar{\varepsilon}^{pl}}{\varepsilon_f^{pl}} \right) \qquad [4]$$

$$\bar{\varepsilon}_f^{pl} = \left[d_1 + d_2 \exp\left(d_3 \frac{p}{q}\right) \right] \left[1 + d_4 \ln\left(\frac{\dot{\bar{\varepsilon}}^{pl}}{\dot{\varepsilon}_0}\right) \right] \left[1 + d_5 \left(\frac{T - T_r}{T_m - T_r}\right) \right] \qquad [5]$$

where d_1 to d_5 are failure parameters measured at or below the transition temperature, p is the pressure stress, q is the Mises equivalent stress, $\dot{\bar{\varepsilon}}^{pl}$ is the equivalent plastic strain rate and $\Delta \bar{\varepsilon}^{pl}$ is the incremental increase in the equivalent plastic strain.

The upper limit of the crack velocities in the oxide layers (Ta_2O_5 and Fe_2O_3) were estimated from the equation for the speed of sound in elastic solid ($v = E/\rho$),[41,50] where E and ρ are the Young's modulus and the density of the oxide layer, respectively. Using this equation, the speed of sound in Ta_2O_5 and Fe_2O_3 were estimated to be 4700 and 5577 ms^{-1}, respectively. Thus, the time required for a dynamic crack to grow through the 2.8 nm thick oxide film is approximately 0.5 ps for both oxide layers. However, a significant temperature rise in the system occurs within nanosecond time scale of impact (see Figure 5). As a result, the rate of crack growth across the oxide layer is much faster than the rate of temperature increase. Thus, it is reasonable
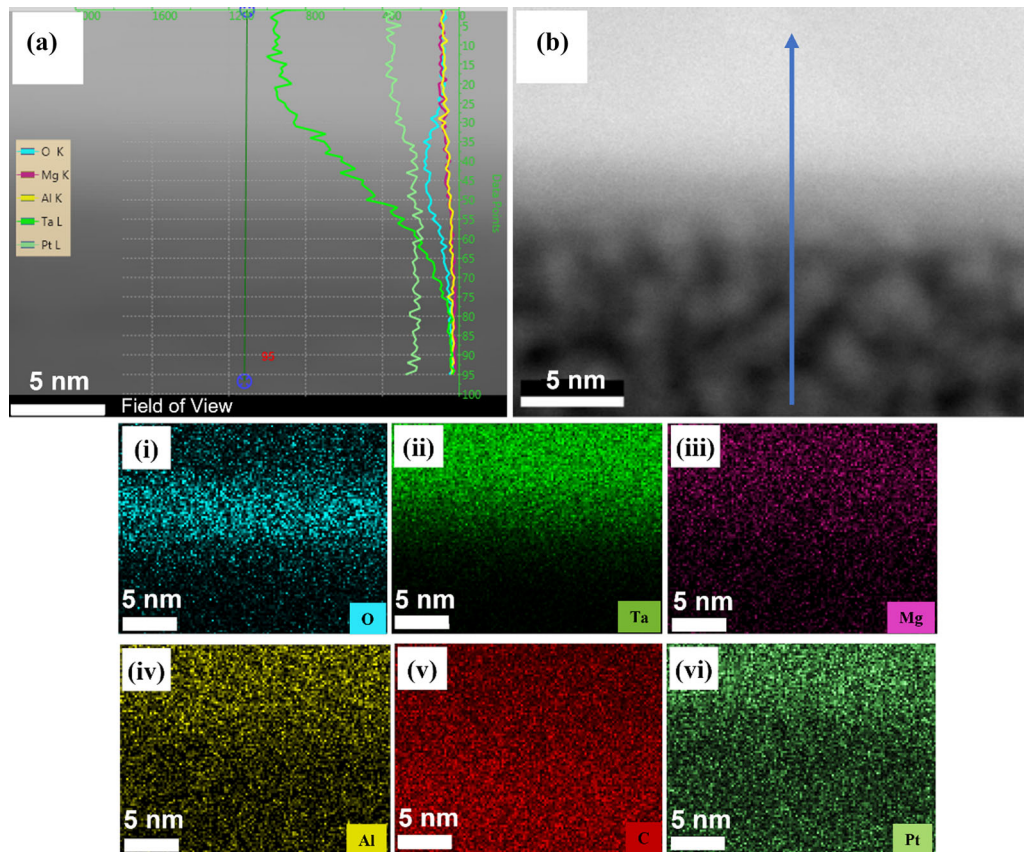
Fig. 3—STEM-EDAX data collected from a FIB-cut cross section through the surface of Ta powder particle: (*a*) line scan data acquired from the position as indicated by the blue arrow in the STEM-HAADF image in (*b*) while (i to vi) are high resolution X-ray maps extracted from (a) showing the distinct oxide layer in the oxygen map (i) (Color figure online).
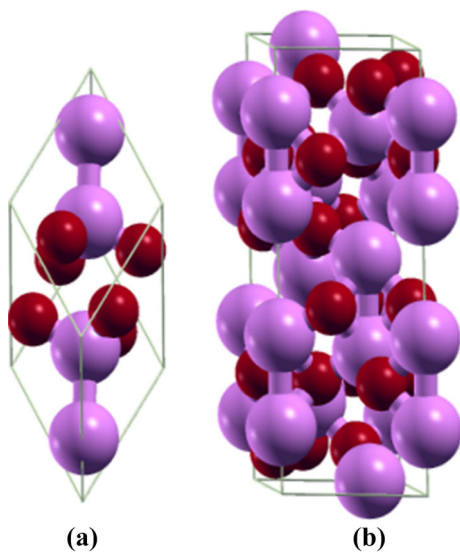

Fig. 4—(Color online) Crystal structures of Fe_2O_3, where the purple and red spheres represent Fe and O atoms, respectively (*a*) Rhombohedral primitive cell of Fe_2O_3. (*b*) Hexagonal unit cell of Fe_2O_3.

Table I. Material Properties

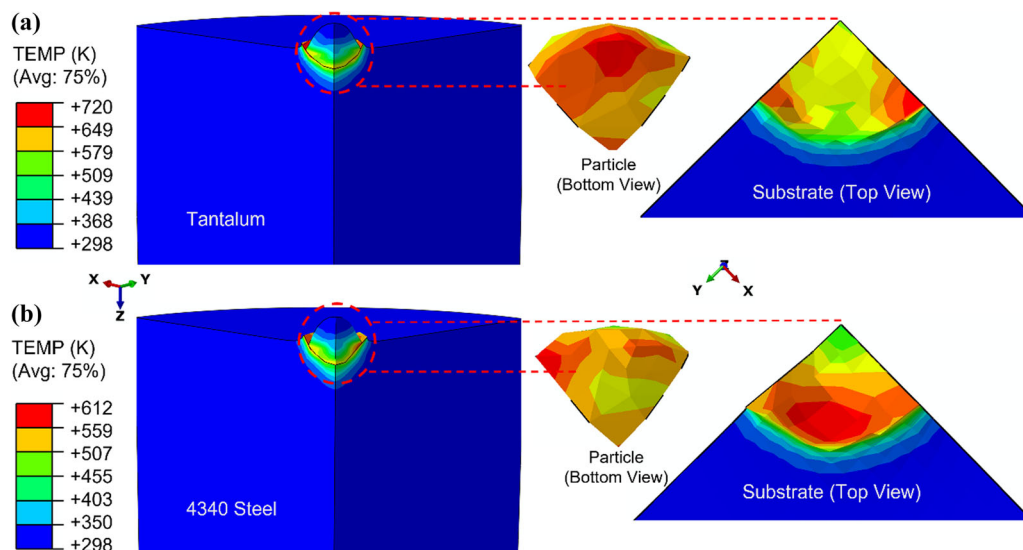|	Tantalum[40,43–46]	4340 Steel[47–49]
A(MPa)	611	792
B(MPa)	704	510
C_1	0.015	0.26
C_2	0.131	0.014
m	0.251	1.03
n	0.608	0.26
$\dot{\varepsilon}_0$	1	1
$\dot{\varepsilon}_c$	1000	1000
d_1	0	0.05
d_2	0.3	3.44
d_3	0.3	− 2.12
d_4	0.6	0.002
d_5	1	0.61
T_{melt} (K)	3269	1793
Density (Kgm^{-3})	16,600	7830
Young's Modulus (GPa)	183	208
Poisson Ratio	0.35	0.3
Specific Heat ($Jkg^{-1} K^{-1}$)	140	477
Inelastic Heat Fraction	0.9	0.9

Fig. 5—(a) Temperature distribution during the cold spray impact of a single Ta particle on Ta substrate (b) Temperature distribution during the cold spray impact of a single Ta particle on 4340 steel substrate.

to assume that brittle cracking is dominant mechanism in comparison to phonon transport and will occur in the oxide layer at temperatures close to the initial temperature (300 K).

Brittle cracking of the top surface oxides was modeled based on the Rankine criterion,[51,52] which assumes the formation of cracks when the principal tensile stress is greater than the tensile strength of the brittle material. Crack initiation in the model was based on the mode I fracture energy, while crack propagation was based on both mode I and mode II fracture energies. The failure stress was taken as the theoretical strength (σ) of the oxide material which was estimated by dividing the Young's modulus value by 10.[53,54] The fraction of the unfractured oxide was calculated by simply dividing the number of failed nodes (based on the damage criteria used for brittle cracking) by the number of un-failed nodes of the shell elements describing the oxide layer in the finite element simulation.

III. RESULTS AND DISCUSSION

A. Mechanical Properties of Nanoscale Oxides on Ta and 4340 Steel

A thin layer of metallic oxide of few nanometers thickness is usually formed on the top surface of metallic powders and substrate. This oxide layer is believed to have a significant impact on the cold spray behavior of metallic materials. In the case of Ta powders, we have observed the presence of an amorphous Ta_2O_5 layer with a thickness of about 2.8 nm on the top surface of the particle, as shown in Figures 2(c) and (d).

Thus, the Ta material in our FEM is considered with an amorphous oxide layer atop. A stable Fe_2O_3 layer is also assumed to be formed on top of the 4340 steel. Although the formation of other oxides, such as wustite and magnetite, is also feasible, hematite was selected for

simplicity. To successfully capture the nanoscale behavior of the Fe_2O_3 top surface oxide layer on 4340 steel, the essential material parameters required for the finite element simulations were obtained from DFT calculations.

The calculated equilibrium lattice parameters for the rhombohedra primitive structure of Fe_2O_3 (a = 5.40, γ = 55.3) are comparable to the previously reported values.[55] The mechanical properties of the Fe_2O_3 are presented in Table II. These calculated properties are consistent with the previously reported values.[56] The properties of the amorphous Ta_2O_5 were obtained from Reference 57.

B. Temperatures Associated with Powder Impact

The high impact in a cold spray process induces heat energy and some of the prior authors have attributed the onset of jetting (a condition necessary for bonding) to this induced heat in a phenomenon referred to as adiabatic shear instability.[40,58] The induced heat leads to a local temperature increase in the region close to the interface between the particle and the substrate. The induced temperature distributions depend on the impact velocity and the thermal properties of the materials.

Figures 5(a) and (b) show multiple views of the temperature distribution profiles (with a 75 pct nodal average in ABAQUS) obtained from our simulations of a single Ta particle impact on a Ta substrate and on a 4340 steel substrate within 30 ns of impact at a deposition speed of 680 ms^{-1}. The different temperature profiles observed for Ta on Ta, and Ta on 4340 steel, are attributed to the differences in both the mechanical and the thermal properties of the materials. The temperature range in Ta on Ta is higher, due to the lower heat capacity of Ta compared to that of 4340 steel. The maximum temperature increase in Ta is far below the melting temperature because Ta is a refractory metal with a high melting temperature of 3269 K.[46] Similarly,

Table II. Lattice Constants and the Mechanical Properties of the 4340 Steel Topical Oxide

	v	E (GPa)	σ (GPa)
Ta_2O_5	0.25	152	15.2
Fe_2O_3	0.22	219	21.9

the maximum temperature rise in steel is below the melting temperature of 1793 K,[59] but above the recrystallization temperature of steel. Hence, diffusion bonding is possible between the Ta particle and the 4340 steel substrate.

C. *Deformation and Cracking*

The dissipation of the particle energy upon impact during a cold spray process induces stress states in the oxide coated particles and substrate. These stress states may reach critical conditions that can cause cracking and shear phenomena at sufficiently high impact. The stress states, cracking and the resulting splat microstructures associated with the cold spray impact of a single Ta particle on a Ta substrate and on a 4340 steel at a deposition velocity of 680 ms^{-1} are presented in Figures 6(a) through (c).

Figures 6(a) and (b) show evidence of cracking of the oxide layers within 10 ns of impact for both Ta on Ta and Ta on 4340 steel and this progresses with time. The stress states at the bottom of the particle during impact causes the particle to undergo a high and rapid plastic deformation which results into the evolution of the splat microstructures that are observed in Figures 6(a) and (b). The corresponding equivalent plastic strains associated with the high impact-induced deformation are presented in Figures 7(a) and (b). The results reveal more susceptibility of the outer contact zone to plastic deformation than the contact region's center. During the contact process, the contact region expands as the maximum equivalent plastic strain evolves, and the substrate surface material accumulates around the contact region. This is consistent with the previous theoretical and experimental results.[60,61] Since the strain associated with the particle impact is only limited to the surface of the substrate, the impact does not have a significant influence on the robustness of the bulk material.

It can be inferred that during the splat evolution, shear stresses extrude materials from the borders of the splats. This extrusion process is also linked to the gradual shear extrusion and fracture of the oxide segments from the splats' surfaces. The stages of deformation and cracking associated with powder particle impact in a cold spray process are illustrated schematically in Figure 6(c). This involves the initial elastic contact of the particles with the substrate, followed by plastic deformation and cracking phenomena in the regions surrounding the resulting splat; shear-controlled extrusion and cracking, the cracking

of the oxide coatings on the particle and the substrate then exposes the bare metal surfaces, which then allow for bonding and geometric interlocking to occur.

The results shown in Figures 6(a) through (c) clearly reveal the presence of some unfractured oxides near the contact regions (the south pole), this behavior of the deposited particle has also been reported for 6061 Al particle of larger size.[41] The bonding of the coating to the substrate has previously been shown to be dependent on metallurgical bonding associated with true metal-to-metal contact achieved by the formation of oxide-free surfaces during jetting.[62] Thus, the unfractured oxides trapped at the interface decrease the actual contact area between the incoming particle and the underlying bare metal substrate surfaces, they reduce the possible areas for bonding to occur between the incident particle and the substrate. The fraction of this unfractured oxide is important in terms of the bonding strength of the cold sprayed structures and depend on several factors such as the impact velocity, oxide thickness and the properties of the materials. The effects of some of these factors will be discussed in the next section.

D. *Effects of Oxide Thickness and Particle Impact Velocity*

We have shown in the previous section that the cracking and the removal of the topical oxides formed on both the particle and the substrate are precursors to the bonding and mechanical interlocking in cold sprayed structures. It has also been shown that some of the oxides may remain unfractured and trapped at the particle/substrate interface. The extent to which the oxide layer will fracture depends on several parameters such as the impact speed, the properties and thickness of the oxides.

The understanding of the effects of the above parameters is crucial for the improvement of the efficiency of a cold spray process. Figures 8(a) and (b) present the effects of particle impact velocity and oxide thickness on the fraction of unbroken oxides. The results show a decrease in the fraction of unfractured oxides with increasing impact velocity. This is consistent with the results obtained in prior studies which show increase in coating strength with increasing particle velocity.[63–65] Similar results are obtained for the effects of oxide thickness shown in Figure 8(b). The results are further corroborated with the inset in Figure 8 which shows the predicted FEM results at some selected spray velocities and oxide thicknesses.

IV. IMPLICATIONS

The above results show that the impact of Ta powders with topical oxide layers can have a significant effect on Ta substrates and 4340 steel substrates (also with topical oxide layers) during the cold spray of Ta powders. The resulting increase in temperature can enhance the deformation of the powders during contact, resulting ultimately in the formation of deformed splats.[66]
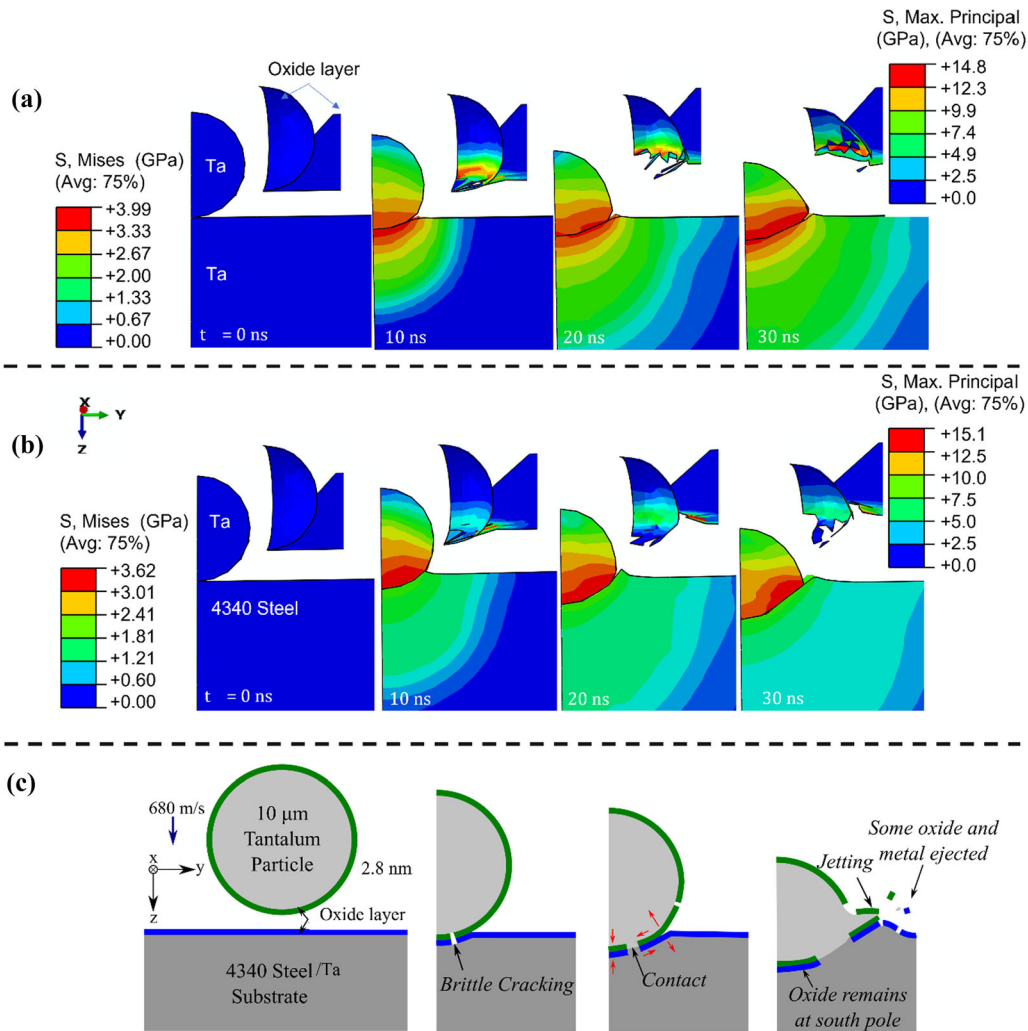
Fig. 6—(top) Cracking of oxide layers with colors corresponding to the maximum principal stress and (bottom) the resulting splat microstructures of the particle on the substrate in cold spray impact of (*a*) Ta particle on Ta substrate. (*b*) Ta particle on 4340 steel substrate with colors corresponding to the Von mises stress on the particle and the substrate. (*c*) Schematic representation of the brittle cracking, splat formation and jetting in a cold spray process (Color figure online).
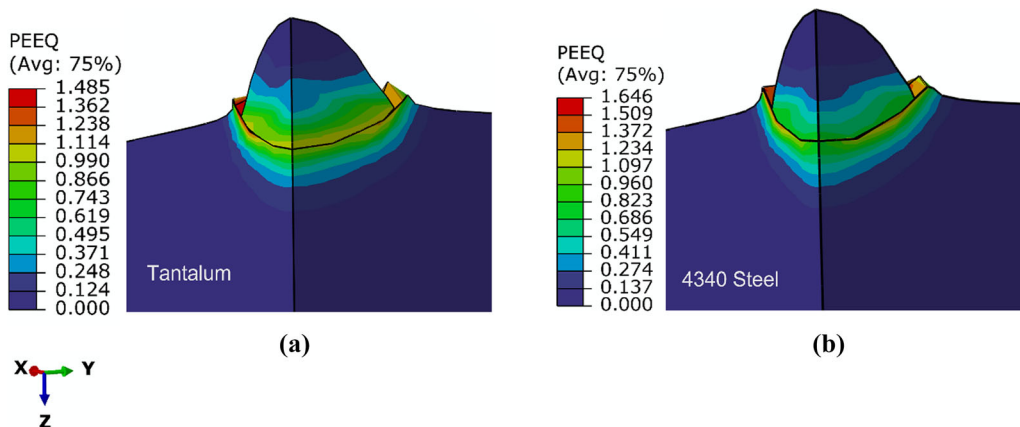

Fig. 7—Equivalent plastic strain for a cold spray impact of 10-*μ*m Ta particle on a (*a*) Ta substrate and on a (*b*) 4340 steel substrate.
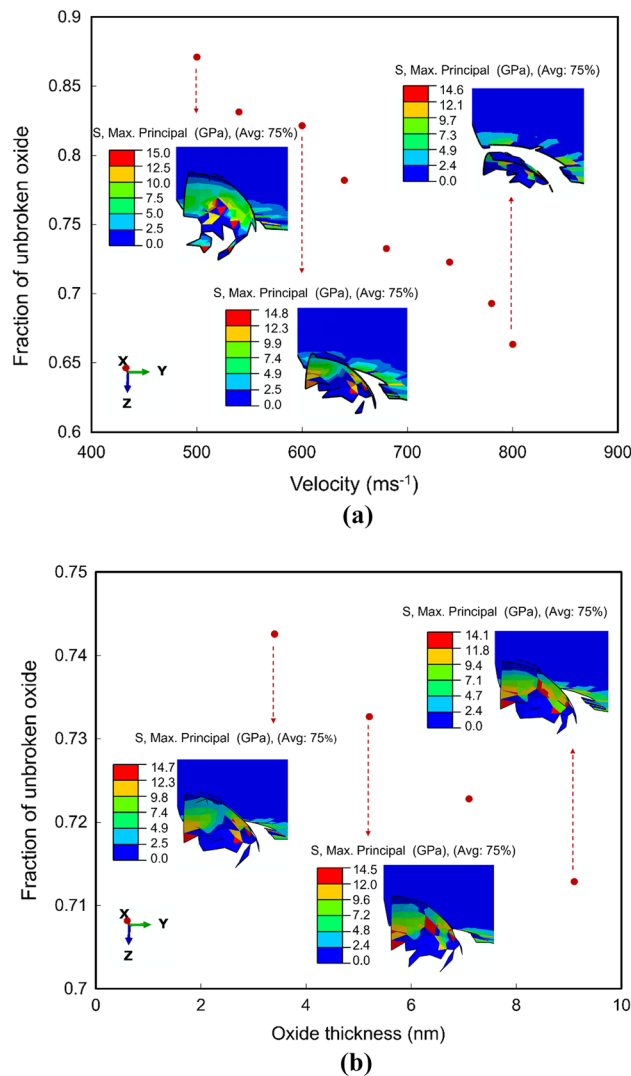
Fig. 8—Effects of (*a*) impact velocity and (*b*) the oxide thickness on the cracking and removal of the topical oxides.

Furthermore, since the temperatures associated with the cold spray contacts may exceed the recrystallization temperature (~ 598 K for 4340 steel and ~ 1090 K for Ta), diffusion phenomena can occur during cold spray processes in which the induced temperature rises exceed the recrystallization temperature.[67] Such temperature rises may be sufficient to promote some diffusion bonding of the Ta powders to the Ta or 4340 steel substrates.

The presence of nanoscale amorphous oxide layer coating on tantalum particles has also been confirmed in this work (Figures 2(a) through (c)). The cracking and removal of this oxide layer in the cold spray impact of Ta powders on Ta or 4340 steel substrate are presented in Figures 6(a) through (c). These have been shown to allow for a strong adhesion or bonding in a cold spray process.[68,69]

Finally, we have shown the presence of some unfractured oxides in the regions of contact that occur during cold spray impact. The fraction of these unfractured oxides depends on factors such as the spray velocity and the oxide thickness (Figure 8). Thus, the current work suggests that the deformation and cracking phenomena that can occur during cold spray processing, provide some important insights for the design of cold spray processing conditions. Further work is clearly needed to study the mechanical properties of the resulting structures. These are clearly opportunities for future work.

V. CONCLUSIONS

We have used a combination of a computational modeling and experiments to study the effects of nanoscale topical oxides and spray velocity on the cold spray impact of Ta particles on Ta substrate or 4340 steel substrates. Our results reveal the presence of amorphous topical Ta_2O_5 layers on Ta particles with a thickness of ~ 2.8 nm. The results obtained also show that the impact-induced temperatures are well above the recrystallization temperature of 4340 steel, which suggests that diffusion bonding can occur during the cold spray processing of Ta particles on 4340 steel substrate. The FEA simulations show the formation of splat microstructures upon powder impact with the Ta/4340 steel substrates. These are accompanied with the cracking of the oxide coatings on the Ta particles and the Ta/4340 steel substrates. The results also show that the incident particle velocity and the Ta oxide thickness are negatively correlated with the fraction of unfractured Ta oxide. The current findings confirm the importance of the deformation and cracking of topical oxide films on the cold spray behavior of Ta powders on Ta or 4340 steel substrates.

AUTHOR CONTRIBUTIONS

RA: Conducting experimental work and simulation, Data analysis, Writing—original draft. VR: Assistance in coding and simulation. TB: Discussion, Assistance in data analysis, Writing—review & editing. MV: Discussion, Assistance in data analysis, Writing—review & editing. JO: Assistance in experiments, Assistance in data analysis, Writing—review & editing. AN: Discussion, Assistance in data analysis, Writing—review & editing. OO: Supervision, Assistance in the experiments, Data analysis, Writing—review & editing. JO: Supervision, Data analysis, Writing—review & editing. NR: Supervision, Data analysis, Writing—review &

editing. WS: Supervision, Data analysis, Funding acquisition, Writing—review & editing.

COMPETING INTEREST

REFERENCES

1. M.F. Smith: *Cold Spray Mater Depos. Process Fundam. Appl.*, 2007, vol. 1911, pp. 43–61.
2. A. Moridi, S.M. Hassani-Gangaraj, M. Guagliano, and M. Dao: *Surf. Eng.*, 2014, vol. 30, pp. 369–95.
3. S. Pathak and G.C. Saha: *Coatings*, 2017, vol. 7, pp. 2079–6412.
4. S. An, B. Joshi, A.L. Yarin, M.T. Swihart, and S.S. Yoon: *Adv. Mater.*, 2020, vol. 32, pp. 1–34.
5. P. Poza and M.Á. Garrido-Maneiro: *Prog. Mater. Sci.*, 2022, vol. 123, p. 100839.
6. J.C. Lee, H.J. Kang, W.S. Chu, and S.H. Ahn: *CIRP Ann.*, 2007, vol. 56, pp. 577–80.
7. V. Champagne and D. Helfritch: *Mater. Sci. Technol.*, 2015, vol. 31, pp. 627–34.
8. S. Sinha-Ray, M.W. Lee, S. Sinha-Ray, S. An, B. Pourdeyhimi, S.S. Yoon, and A.L. Yarin: *J. Mater. Chem. C*, 2013, vol. 1, pp. 3491–98.
9. S. An, C. Lee, M. Liou, H.S. Jo, J.-J. Park, A.L. Yarin, and S.S. Yoon: *ACS Appl. Mater. Interfaces*, 2014, vol. 6, pp. 13657–66.
10. D.Y. Kim, J.J. Park, J.G. Lee, D. Kim, S.J. Tark, S. Ahn, J.H. Yun, J. Gwak, K.H. Yoon, S. Chandra, and S.S. Yoon: *J. Therm. Spray Technol.*, 2013, vol. 22, pp. 1092–1102.
11. B. Kang, K.D. Lee, J.-G. Lee, J.-W. Choi, S.S. Yoon, Y. Kang, H.-S. Lee, and D. Kim: *J. Therm. Spray Technol.*, 2016, vol. 25, pp. 465–72.
12. J.G. Lee, B.N. Joshi, J.H. Lee, T.G. Kim, D.Y. Kim, S.S. Al-Deyab, I.W. Seong, M.T. Swihart, W.Y. Yoon, and S.S. Yoon: *Electrochim. Acta*, 2017, vol. 228, pp. 604–10.
13. E. Samuel, J.G. Lee, B. Joshi, T.G. Kim, M.W. Kim, I.W. Seong, W.Y. Yoon, and S.S. Yoon: *J. Alloys Compd.*, 2017, vol. 715, pp. 161–69.
14. B. Joshi, J.G. Lee, E. Samuel, H.S. Jo, T.G. Kim, M.T. Swihart, W.Y. Yoon, and S.S. Yoon: *J. Alloys Compd.*, 2017, vol. 726, pp. 114–20.
15. T.G. Kim, E. Samuel, B. Joshi, C.W. Park, M.W. Kim, M.T. Swihart, W.Y. Yoon, and S.S. Yoon: *J. Alloys Compd.*, 2018, vol. 766, pp. 331–40.
16. J.G. Lee, D.Y. Kim, B. Kang, D. Kim, S.S. Al-Deyab, S.C. James, and S.S. Yoon: *Comput. Mater. Sci.*, 2015, vol. 108, pp. 114–20.
17. H. Assadi, H. Kreye, F. Gärtner, and T. Klassen: *Acta Mater.*, 2016, vol. 116, pp. 382–407.
18. M. Hassani-Gangaraj, D. Veysset, V.K. Champagne, K.A. Nelson, and C.A. Schuh: *Acta Mater.*, 2018, vol. 158, pp. 430–39.
19. M. Hassani-Gangaraj, D. Veysset, K.A. Nelson, and C.A. Schuh: *Appl. Surf. Sci.*, 2019, vol. 476, pp. 528–32.
20. C.-J. Li, H.-T. Wang, Q. Zhang, G.-J. Yang, W.-Y. Li, and H.L. Liao: *J. Therm. Spray Technol.*, 2009, vol. 19, pp. 95–101.
21. Y. Ichikawa, K. Ogawa, Y. Ichikawa, and K. Ogawa: *JTST*, 2015, vol. 24, pp. 1269–76.
22. K.H. Kim, W. Li, and X. Guo: *Appl. Surf. Sci.*, 2015, vol. 357, pp. 1720–26.
23. Y. Xie, S. Yin, C. Chen, M.P. Planche, H. Liao, and R. Lupoi: *Scr. Mater.*, 2016, vol. 125, pp. 1–4.
24. Y. Ichikawa, R. Tokoro, M. Tanno, and K. Ogawa: *Acta Mater.*, 2019, vol. 164, pp. 39–49.
25. J. Lienhard, C. Crook, M.Z. Azar, M. Hassani, D.R. Mumm, D. Veysset, D. Apelian, K.A. Nelson, V. Champagne, A. Nardi, C.A. Schuh, and L. Valdevit: *Acta Mater.*, 2020, vol. 197, pp. 28–39.
26. B. Barnett, M. Trexler, and V. Champagne: *Int. J. Refract. Met. Hard Mater.*, 2015, vol. 53, pp. 139–43.
27. A. Nifa, L. Berthe, M. Boustie, L.L. Descurninges, M. Jeandin, J. Bénier, and P. Mercier: *Int. Congr. Appl. Lasers Electro-Opt.*, 2018, vol. 2012, p. 633.
28. J.V.S.N. Sripada, M.F. Gallant, G.C. Saha, R. Singh, and J. Kondas: *Key Eng. Mater.*, 2019, vol. 813, pp. 429–34.
29. S.M. Cardonne, P. Kumar, C.A. Michaluk, and H.D. Schwartz: *Int. J. Refract. Met. Hard Mater.*, 1995, vol. 13, pp. 187–94.
30. P.F. Weck and E. Kim: *Phys. Chem. Chem. Phys*, 2016, vol. 18, pp. 26816–26.
31. R. Sakanoi, T. Shimazaki, J. Xu, Y. Higuchi, N. Ozawa, K. Sato, T. Hashida, and M. Kubo: *J. Chem. Phys.*, 2014, vol. 140, p. 121102.
32. Y.N. Wu, L. Li, and H.P. Cheng: *Phys. Rev. B*, 2011, vol. 83, p. 144105.
33. P. Giannozzi, S. Baroni, N. Bonini, M. Calandra, R. Car, C. Cavazzoni, D. Ceresoli, G. Chiarotti, M. Cococcioni, I. Dabo, A. Dal Corso, S. de Gironcoli, S. Fabris, G. Fratesi, R. Gebauer, U. Gerstmann, C. Gougoussis, A. Kokalj, M. Lazzeri, L. Martin-Samos, N. Marzari, F. Mauri, R. Mazzarello, S. Paolini, A. Pasquarello, L. Paulatto, C. Sbraccia, S. Scandolo, G. Sclauzero, A. Seitsonen, A. Smogunov, P. Umari, and R. Wentzcovitch: *J. Phys.*, 2009, vol. 21, p. 395502.
34. R. Ovcharenko, E. Voloshina, and J. Sauer: *Phys. Chem. Chem. Phys.*, 2016, vol. 18, pp. 25560–68.
35. F. Kraushofer, Z. Jakub, M. Bichler, J. Hulva, P. Drmota, M. Weinold, M. Schmid, M. Setvin, U. Diebold, P. Blaha, and G.S. Parkinson: *J. Phys. Chem. C*, 2018, vol. 122, pp. 1657–69.
36. H. Assadi, F. Gärtner, T. Stoltenhoff, and H. Kreye: *Acta Mater.*, 2003, vol. 51, pp. 4379–94.
37. T. Schmidt, F. Gärtner, H. Assadi, and H. Kreye: *Acta Mater.*, 2006, vol. 54, pp. 729–42.
38. M. Hassani-Gangaraj, D. Veysset, K.A. Nelson, and C.A. Schuh: *Scripta Mater.*, 2018, vol. 145, pp. 9–13.
39. G.Z. Voyiadjis and F.H. Abed: *Mech. Mater.*, 2005, vol. 37, pp. 355–78.
40. J.B. Kim and H. Shin: *Int. J. Impact Eng.*, 2009, vol. 36, pp. 746–53.
41. A. Navabi, M. Vandadi, T. Bond, V. Rahneshin, J. Obayemi, R. Ahmed, J.E. Oghenevweta, V. Champagne, N. Rahbar, and W.O. Soboyejo: *Mater. Sci. Eng. A*, 2022, vol. 841, p. 143036.
42. V. Lemiale, P.C. King, M. Rudman, M. Prakash, P.W. Cleary, M.Z. Jahedi, and S. Gulizia: *Surf. Coat. Technol.*, 2014, vol. 254, pp. 121–30.
43. D.G. Westlake: *Scr. Metall.*, 1977, vol. 11, pp. 689–92.
44. Z.L. Kowalewski, Z. Nowak, and R.B. Pęcherski: 1999, pp. 174–83.
45. A. Dorogoy and D. Rittel: *Mech. Mater.*, 2017, vol. 112, pp. 143–53.
46. J.P. Delplanque, W.D. Cai, R.H. Rangel, and E.J. Lavernia: *Acta Mater.*, 1997, vol. 45, pp. 5233–43.
47. G.R. Johnson and W.H. Cook: .@Inproceedings {Johnson2018ACM}.
48. Y.B. Guo and D.W. Yen: *J. Mater. Process. Technol.*, 2004, vol. 155–156, pp. 1350–56.
49. T. Özel and E. Zeren: *Int. J. Adv. Manuf. Technol.*, 2006, vol. 35, pp. 255–67.
50. L.E. Kinsler, A.R. Frey, A.B. Coppens, and J.V. Sanders: Wiley, New York, 1999, p. 560.
51. W.J. Rankine II.: *Philos. Trans. R. Soc. Lond.*, 1857, vol. 147, pp. 9–27.
52. A cracking model for concrete and other brittle materials, https://abaqus-docs.mit.edu/2017/English/SIMACAETHERefMap/simathe-c-cracking.htm, (Accessed 26 December 2021).
53. H.C. Thomas: *Mechanical Behavior of Materials*, Waveland Press, Long Grove, 2005.
54. Z.H.J.C.T. Sun: *Fracture Mechanics*, Academic Press, Waltham, 2012.
55. Y. Guo, S.J. Clark, and J. Robertson: *J. Phys. Condens. Matter*, 2012, vol. 24, p. 325504.
56. P. Liao and E.A. Carter: *J. Mater. Chem.*, 2010, vol. 20, pp. 6703–19.

57. M.R. Abernathy, J.E. Faller, J. Hough, O. Hudson, C. Lynn, I.W. Martin, M. Oyen, S. Rowan, T. Shean, and D. Strange: *Appl. Opt.*, 2014, vol. 53, pp. 3196–3202.
58. M. Grujicic, C.L. Zhao, W.S. DeRosset, and D. Helfritch: *Mater. Des.*, 2004, vol. 25, pp. 681–88.
59. S. Sulaiman, A. Roshan, and M.K.A. Ariffin: *IOP Conf. Ser. Mater. Sci. Eng.*, 2013, vol. 50, p. 012040.
60. S. Dosta, G. Bolelli, A. Candeli, L. Lusvarghi, I.G. Cano, and J.M. Guilemany: *Acta Mater.*, 2017, vol. 124, pp. 173–81.
61. J. Xie, D. Nélias, H.W. Le Berre, K. Ogawa, and Y. Ichikawa: *J. Tribol.*, 2015, vol. 137, p. 041101.
62. T. Hussain, D.G. Mccartney, P.H. Shipway, and D. Zhang: *J. Therm. Spray Technol.*, 2009, vol. 18, pp. 364–79.
63. S. Singh, R.K.S. Raman, C.C. Berndt, and H. Singh: *Metals*, 2021, vol. 11, p. 12.
64. M. Kamaraj and V.M. Radhakrishnan: *J. Therm. Spray Technol.*, 2019, vol. 28, pp. 756–68.
65. H. Assadi, T. Schmidt, H. Richter, J.-O. Kliemann, K. Binder, F. Gärtner, T. Klassen, and H. Kreye: *J. Therm. Spray Technol.*, 2011, vol. 20, pp. 1161–76.
66. W.-Y. Li, C. Zhang, C.-J. Li, and H. Liao: *J. Therm. Spray Technol.*, 2009, vol. 18, p. 921.
67. H. Masumoto, A. Asa'da, H. Hasuyama, K. Nishio, M. Kato, and S. Mukae: *Weld. Int.*, 2010, vol. 11, pp. 110–20.
68. A. Fardan, C.C. Berndt, and R. Ahmed: *Surf. Coat. Technol.*, 2021, vol. 409, p. 126835.
69. A.A. Hemeda, C. Zhang, X.Y. Hu, D. Fukuda, D. Cote, I.M. Nault, A. Nardi, V.K. Champagne, Y. Ma, and J.W. Palko: *Addit. Manuf.*, 2021, vol. 37, p. 101517.